Cell Reports
Physical Science

CellPress
OPEN ACCESS

Article

# Regulating $C_2H_2/CO_2$ adsorption selectivity by electronic-state manipulation of iron in metal-organic frameworks

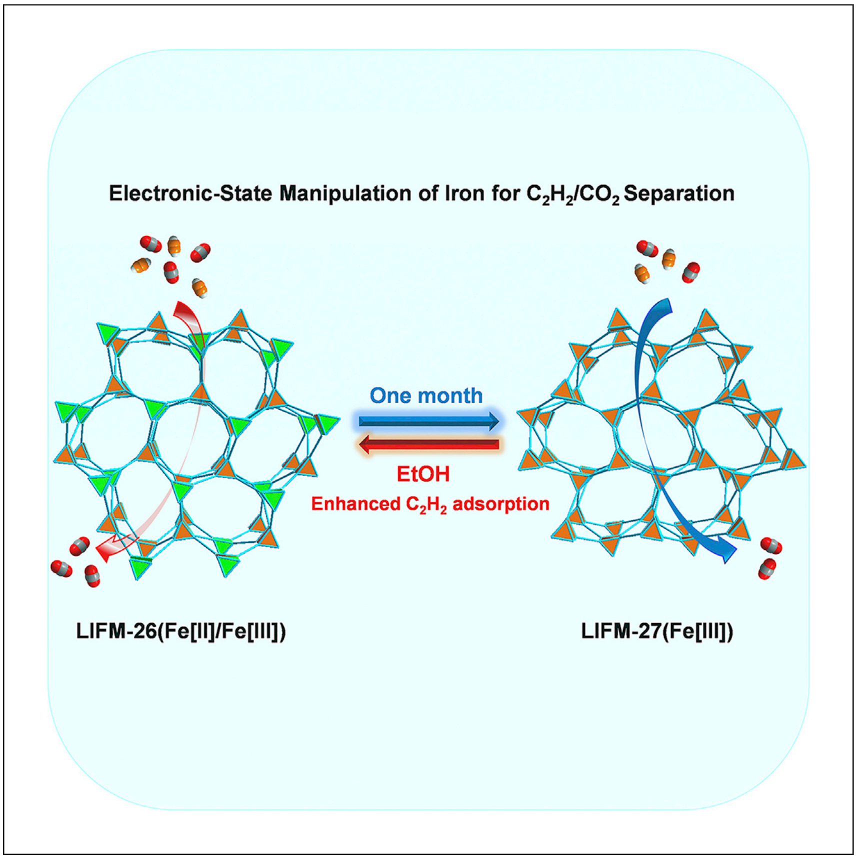

Chen et al. report a metal electronic-state manipulation strategy to construct a pair of isostructural and interconvertible Fe-MOFs featuring open Fe centers with different electron densities for efficient $C_2H_2/CO_2$ separation. They show that the presence of Fe[II] centers with a medium-spin-state trail plays a crucial role in the enhanced $C_2H_2$ selective adsorption.

Cheng-Xia Chen, Tony Pham,
Kui Tan, ..., Lei Zhang,
Cheng-Yong Su, Shengqian Ma

cesscy@mail.sysu.edu.cn (C.-Y.S.)
Shengqian.Ma@unt.edu (S.M.)

## Highlights

The electronic state of Fe can be purposely tuned to regulate $C_2H_2/CO_2$ separation

Increasing electron density of Fe centers results in enhanced $C_2H_2$ adsorption

The interconvertible nature deepens understanding of structure-property relationship

Distinct adsorption mechanism is unveiled through *in situ* FTIR and molecular simulation

Chen et al., Cell Reports Physical Science 3, 100977
August 17, 2022 © 2022 The Author(s).
https://doi.org/10.1016/j.xcrp.2022.100977

Cell Reports
Physical Science

Article

# Regulating $C_2H_2/CO_2$ adsorption selectivity by electronic-state manipulation of iron in metal-organic frameworks

Cheng-Xia Chen,[1,2] Tony Pham,[3] Kui Tan,[4] Rajamani Krishna,[6] Pui Ching Lan,[2] Longfei Wang,[1] Songbo Chen,[7] Abdullah M. Al-Enizi,[8] Ayman Nafady,[8] Katherine A. Forrest,[3] Haiping Wang,[2] Sicheng Wang,[2] Chuan Shan,[3] Lei Zhang,[5] Cheng-Yong Su,[1,9,*] and Shengqian Ma[2,9,*]

## SUMMARY

**The separation of $C_2H_2$ from $C_2H_2/CO_2$ mixture is of great importance, yet highly challenging in the petrochemical industry due to their similar physicochemical properties. While open-metal sites (OMSs) in metal-organic frameworks (MOFs) are known to possess high affinity toward $C_2H_2$, its selective adsorption performance regulated by the electronic state of the same OMSs remains unexplored. Here, we report a metal electronic-state manipulation approach to construct a pair of isostructural Fe-MOFs, namely LIFM-26(Fe[II]/Fe[III]) and LIFM-27(Fe[III]) with different Fe[II] or Fe [III] oxidation states on the Fe centers, which display mixed-valent Fe[II]/Fe[III] centers in the former and sole Fe[III] centers in the latter. Remarkably, LIFM-26(Fe[II]/Fe[III]) shows significantly enhanced $C_2H_2$ uptake capacity than LIFM-27(Fe[III]), attested by adsorption isotherms and IAST calculations, as well as simulated and experimental breakthrough experiments. Furthermore, *in situ* infrared (IR) and molecular calculations unveil that the presence of Fe[II] in LIFM-26(Fe[II]/Fe[III]) results in stronger Fe[II]–$C_2H_2$ interactions than Fe[III]–$C_2H_2$, which plays a key role in the $C_2H_2/CO_2$ separation.**

## INTRODUCTION

Industrial chemical separations account for 10%–15% of the global energy consumption, which corresponds to half of the United States's industrial energy use.[1] Among them, acetylene ($C_2H_2$) purification represents an energy- and cost-intensive process.[2] As one of the most widely used feedstocks in the petroleum industry, $C_2H_2$ is mainly produced by the combustion of methane or thermal cracking of petroleum, with $CO_2$ as the major byproduct.[3] Therefore, separating $CO_2$ from $C_2H_2/CO_2$ gas mixture is of great importance. Presently, the industrial separation of $CO_2$ from $C_2H_2$ is usually implemented through solvent extraction and cryogenic distillation, leading to intensive costs and energy penalties due to their similar physicochemical properties (molecular sizes and shapes: $3.32 \times 3.34 \times 5.70$ Å$^3$ for $C_2H_2$, $3.18 \times 3.33 \times 5.36$ Å$^3$ for $CO_2$; boiling points: 189.3 and 194.7 K for $C_2H_2$ and $CO_2$, respectively).[4,5] As a result, adsorptive separation based on porous solid materials has drawn much attention owing to the advantage of dramatically reducing the energy and cost consumption.[6–10]

Owing to their structural diversity, designable pore size, high pore volume, and tunable functionalities, metal-organic frameworks (MOFs) have shown great

[1] MOE Laboratory of Bioinorganic and Synthetic Chemistry, Lehn Institute of Functional Materials, School of Chemistry, Sun Yat-Sen University, Guangzhou 510275, China

[2] Department of Chemistry, University of North Texas, Denton, TX 76201, USA

[3] Department of Chemistry, University of South Florida, Tampa, FL 33620, USA

[4] Department of Materials Science & Engineering, University of Texas at Dallas, Richardson, TX 75080, USA

[5] College of Materials Science and Engineering, Fujian University of Technology, Fuzhou 350118, China

[6] Van't Hoff Institute for Molecular Sciences, University of Amsterdam, 1098 Amsterdam, the Netherlands

[7] School of Physical Science and Technology, Lanzhou University, Lanzhou 730000, China

[8] Department of Chemistry, College of Science, King Saud University, Riyadh 11451, Saudi Arabia

[9] Lead contact

*Correspondence:
cesscy@mail.sysu.edu.cn (C.-Y.S.),
Shengqian.Ma@unt.edu (S.M.)

https://doi.org/10.1016/j.xcrp.2022.100977

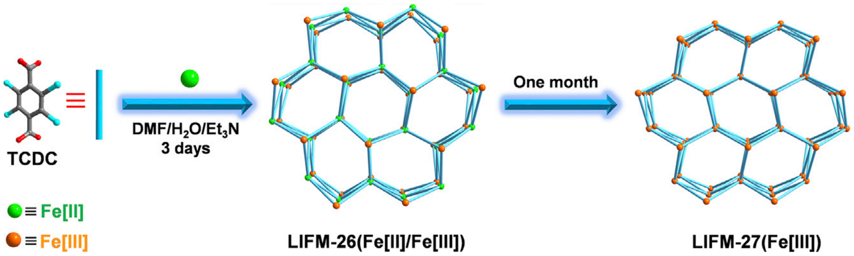

**Scheme 1. Schematic synthetic route of Fe-MOF isostructures with different ratios of Fe[II] and Fe[III] centers through a metal electronic-state manipulation strategy**

potentials in gas adsorption and separation involving $C_2H_2/CO_2$, $C_2H_4/C_2H_6$, $C_3H_6/C_3H_8$, $N_2/O_2$, $CO/H_2$, and $CO/N_2$.[8–15] However, it is still challenging to rationally design MOFs for $C_2H_2/CO_2$ separation due to their similar dynamic sizes and volatility. Tremendous efforts have been devoted to developing highly effective MOF adsorbents, suggesting that the introduction of open-metal sites (OMSs) into suitable pore space is most likely to be competent for this task.[16–24] The suitable pore space (appropriate pore size, high pore volume, and polar pore surface) can render the framework with a high $C_2H_2$ adsorption working capacity and facilitates adsorption dynamics.[25–30] In addition, the OMSs with exposed partial positive charges not only behave as Lewis-acid-accepting electrons from the electron lone pair orbital of $C_2H_2$ but also function as a $\pi$-bond back donor providing electrons to $C_2H_2$ (delocalizing d electrons to the antibonding $\pi^*$ orbitals of $C_2H_2$), thus resulting in preferential adsorption toward $C_2H_2$ over $CO_2$.[26,31–33] However, it is extremely difficult to combine exposed positive charges and strong $\pi$ back donors into a single material. Actually, most MOFs with OMSs present weak $\pi$-bond back donation due to their electron-poor metal centers, and only a few MOFs featuring exposed electron-rich metal centers are found to be suitable for $\pi$-bond back donation.[32,34–36]

In order to functionalize MOFs with electron-rich OMSs for highly selective $C_2H_2$ adsorption, it is anticipated that the manipulation of the mixed-valent electronic states of exposed metal centers in a suitable MOF pore space is an effective yet challenging strategy. The introduction of an appropriate low-valent metal center can impart enhanced $\pi$ back donation, thereby facilitating the preferential $C_2H_2$ adsorption over $CO_2$, while the presence of a high-valent metal center can allow for facile desorption of $C_2H_2$ due to the moderate metal-adsorbate interactions. Herein, we report a pair of isostructural Fe-MOFs, namely LIFM-26(Fe[II]/Fe[III])[37] and LIFM-27(Fe[III]) (LIFM stands for Lehn Institute of Functional Materials) that possess pore spaces constructed from the same perchlorinated ligand (2,3,5,6-tetrachloride terephthalic acid [TCDC]) (Scheme S1) and oxidation-state variant Fe[II]/Fe[III] centers (Scheme 1). Both structures feature coordinately unsaturated Fe centers, in which the ratios of Fe[II] and Fe[III] can be purposely tuned through an *in situ* redox process (Scheme 1), endowing the isostructural Fe-MOFs with distinct $C_2H_2$ selective adsorption performance. It is worth noting that LIFM-26(Fe[II]/Fe[III]) and LIFM-27(Fe[III]) are interconvertible as the isostructures of $(Fe[II]/Fe[III])_3O(TFBDC)_3$ (TFBDC = 2,3,5,6-tetrafluorobenzene-1,4-dicarboxylate),[38] providing ideal examples for studying the inherent relationship between the metal electronic-state and adsorption performance. Compared with LIFM-27(Fe[III]), the increased electron density in LIFM-26(Fe[II]/Fe[III]) affords much higher $C_2H_2$ uptake capacity and superior $C_2H_2$ selectivity over $CO_2$ in the low-pressure region, due to the stronger Fe[II]-adsorbate interactions than Fe[III]-$C_2H_2$, which illustrates that manipulation of the electronic-state of OMSs can lead to enhanced preferential $C_2H_2$ adsorption.

Moreover, the combined studies of ideal adsorbed solution theory (IAST) calculations, simulated/experimental dynamic breakthrough experiments, molecular simulations, and *in situ* infrared (IR) analysis well confirm that the exposed Fe[II] center with a strong $\pi$ back-donation character plays a crucial role in the enhanced $C_2H_2$/$CO_2$ separation.

## RESULTS AND DISCUSSION

### Synthesis and structure determination

LIFM-26(Fe[II]/Fe[III]) was synthesized according to our previously reported method with a slight modification.[37] The slow diffusion of triethylamine vapor into a mixture of *N*,*N*′-dimethylformamide (DMF) and water dissolving TCDC ligand and $FeCl_2$ for 3 days afforded LIFM-26(Fe[II]/Fe[III]) crystals, during which Fe[II] was partially oxidized into Fe[III]. In comparison, LIFM-27(Fe[III]) was obtained by extending the vapor diffusion time to 1 month, during which Fe[II] was completely oxidized into Fe[III] (Scheme 1). Notably, LIFM-27(Fe[III]) can be transformed back to LIFM-26(Fe[II]/Fe[III]) via soaking the samples in ethanol solution for 3 days at 75°C (denoted as LIFM-27(Fe[III])-EtOH; Figure S10), showing solvent-dependent redox property. Single-crystal X-ray diffraction (SCXRD) analyses reveal that LIFM-26(Fe[II]/Fe[III]) and LIFM-27(Fe[III]) crystalize in the *P*-3 and *P*21/n space groups, respectively (Table S1). Both of them possess the same acs net topology as $(Fe[II]/Fe[III])_3O(TFBDC)_3$, which is constructed from perfluorinated ligand TFBDC and $FeCl_2$ (Figure 1). Compared with $(Fe[II]/Fe[III])_3O(TFBDC)_3$, the $Fe_3O$ clusters in LIFM-26(Fe[II]/Fe[III]) and LIFM-27(Fe[III]) are twisted without the $C_3$ axis of symmetry perpendicular to the $Fe_3O$ plane due to the large steric hindrance of chlorine atoms. The Fe-($\mu_3$-O)-Fe angles in LIFM-26(Fe[II]/Fe[III]) are 115.8°, 120.9°, and 123.3°, while those in LIFM-27(Fe[III]) are 118.4°, 118.8°, and 122.8°. In these three structures, every $Fe_3O$ cluster connects six ligands, whereas every ligand links two independent $Fe_3O$ clusters, thus forming a three-dimensional (3D) framework containing 1D channels (Figures 1C–1E). Notably, $(Fe[II]/Fe[III])_3O(TFBDC)_3$ presents one type of round channel along the c axis with an aperture size of ca. 13.2 Å (Figures 1C and 1F), while LIFM-26(Fe[II]/Fe[III]) features two types of different channels functionalized by chlorine atoms along the c axis, i.e., one round channel with an aperture size of ca. 9.0 Å and one elliptic channel with a pore size of ca. $8.2 \times 11.5$ Å$^2$ (Figures 1D, 1G, and S1). As for LIFM-27(Fe[III]), there is one type of elliptic channel decorated by chlorine atoms along the c axis with a pore size of about $7.5 \times 9.7$ Å$^2$ (Figures 1E, 1H, and S2). Additionally, all three frameworks present one type of tetrahedral cage (diameter ca. 7.0 Å) constructed from six ligands and five $Fe_3O$ clusters (Figure 1I).

In order to probe the oxidation and spin states of Fe centers, $^{57}$Fe Mössbauer spectroscopic experiments were carried out for LIFM-26(Fe[II]/Fe[III]), LIFM-27(Fe[III]), and LIFM-27(Fe[III])-EtOH (Figures 2 and S3–S5; Table S2). The spectra of LIFM-26(Fe[II]/Fe[III]) can be fitted by one type of doublet and one type of singlet, revealing two kinds of Fe species with adsorption area ratios of 47.65% and 52.35%, corresponding to the amounts of Fe[II] and Fe[III] centers (0.9:1.0) (Figure 2A, D1 line). For comparison, only one type of fitting doublet in LIFM-27(Fe[III]) was observed, confirming the existence of sole Fe[III] species (Figure 2B). LIFM-27(Fe[III])-EtOH also shows two kinds of Fe species similar to LIFM-26(Fe[II]/Fe[III]) yet with different adsorption area ratios, implying a variation of Fe[II] and Fe[III] species (Fe[II]:Fe[III] = 0.5:1.0; Figure S5). As shown in Figure 2A, the D2 line can readily be assigned to high-spin Fe[III] species in LIFM-26(Fe[II]/Fe[III]) with isomer shift $\delta = 0.78$ mm/s,[34] while the D3 line can be assigned to medium-spin Fe[II] species with isomer shift $\delta = 0.31$ mm/s and quadrupole splitting value

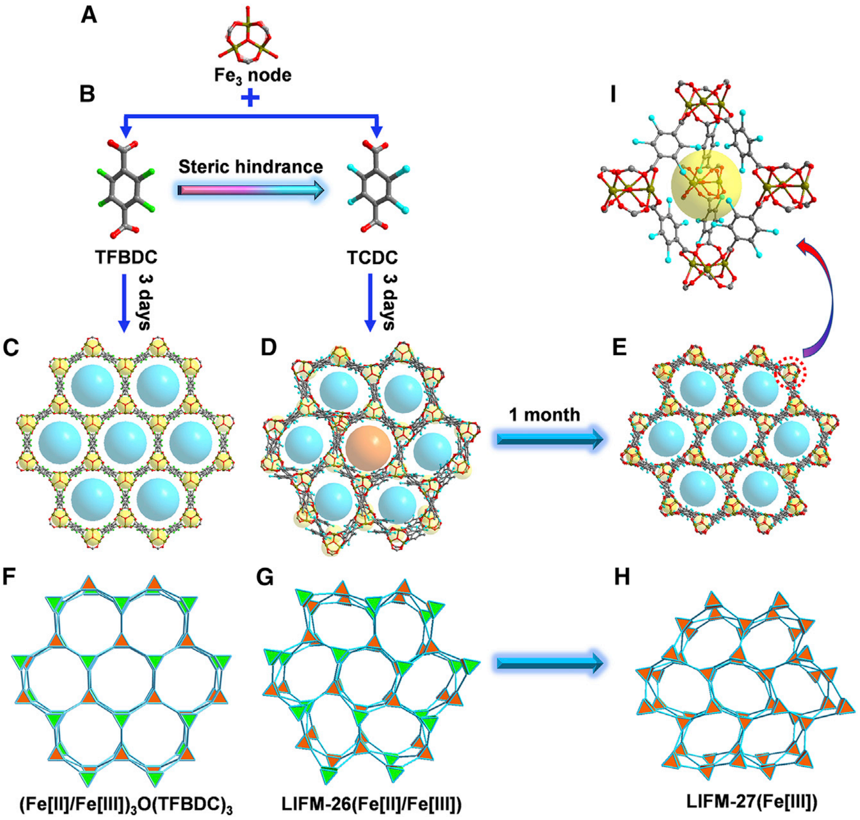

**Figure 1. The schematic construction route of the 3D-MOFs**

(A) Trimeric $Fe_3O$ cluster.

(B) TFBDC and TCDC ligands.

(C–E) The 3D structures of (C) (Fe[II]/Fe[III])$_3$O(TFBDC)$_3$, (D) LIFM-26(Fe[II]/Fe[III]), and (E) LIFM-27(Fe[III]).

(F–H) The corresponding network topologies of (F) (Fe[II]/Fe[III])$_3$O(TFBDC)$_3$, (G) LIFM-26(Fe[II]/Fe[III]), and (H) LIFM-27(Fe[III]).

(I) The tetrahedral cage in three isostructural MOFs.

$\Delta E_Q$ = 0.56 mm/s,[34] suggesting the existence of a strong $\pi$ back donation in LIFM-26(Fe[II]/Fe[III]). For LIFM-27(Fe[III]), the Mössbauer spectra reveal only one type of high-spin Fe[III] species with isomer shift $\delta$ = 0.44 mm/s.

## Purity and porosity

Powder X-ray diffraction (PXRD) patterns were conducted to confirm the phase purity of the as-synthesized samples (Figures S8, S9, and S11), and the scanning electron microscope (SEM) images unveil similar crystal morphology (Figure S7). Thermal gravimetric analyses (TGAs) indicate comparable thermal stability of two isostructural MOFs up to 250°C (Figure S6). In contrast to (Fe[II]/Fe[III])$_3$O(TFBDC)$_3$ (Figure S11), both LIFM-26(Fe[II]/Fe[III]) and LIFM-27(Fe[III]) retain good crystallinity after activation under high vacuum, indicative of their good framework robustness (Figures S8 and S9). $N_2$ sorption isotherms at 77 K were collected to evaluate the permanent porosity of all three samples. As shown in Figure 3A, LIFM-26(Fe[II]/Fe[III]) (356 cm$^3$ g$^{-1}$) and LIFM-27(Fe[III]) (310 cm$^3$ g$^{-1}$) show much higher $N_2$ uptakes than (Fe[II]/Fe[III])$_3$O(TFBDC)$_3$ (17 cm$^3$ g$^{-1}$) due to loss of its crystallinity after activation (Figure S11). Both LIFM-26(Fe[II]/Fe[III]) and LIFM-27(Fe[III]) show typical type I adsorption isotherms with the Brunauer-Emmett-Teller (BET) surface areas of 1,403 and 1,174 m$^2$ g$^{-1}$, respectively, and the total pore volumes are 0.55 and 0.48 cm$^3$ g$^{-1}$, respectively (Figures S12–S14; Table S3). The pore sizes of

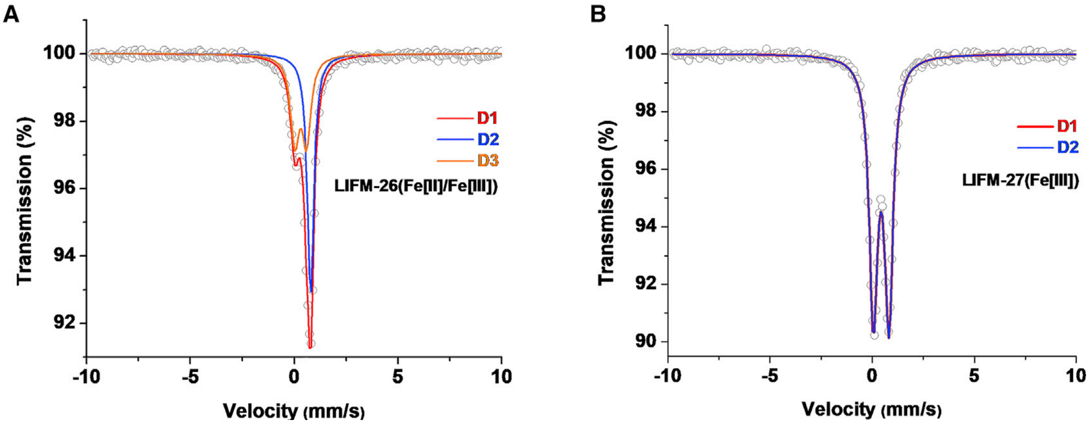

**Figure 2. The $^{57}$Fe Mössbauer Spectroscopy collected at 298 K**
(A) LIFM-26(Fe[II]/Fe[III]).
(B) LIFM-27(Fe[III]).

LIFM-26(Fe[II]/Fe[III]) are calculated to be 6.8, 8.0, and 10.1 Å by density functional theory (DFT) analysis, while those of LIFM-27(Fe[III]) are 6.8 and 8.0 Å (Figure S15), matching well with the corresponding structural analyses. Additionally, we also evaluated the porosity of LIFM-27(Fe[III])-EtOH, which exhibits the BET surface area and pore volumes of 1,330 $m^2$ $g^{-1}$ and 0.53 $cm^3$ $g^{-1}$, falling between those of LIFM-26(Fe[II]/Fe[III]) and LIFM-27(Fe[III]) (Figure S16; Table S4).

## Adsorption studies

The suitable pore structures of two isostructural Fe-MOFs as described above, including appropriate pore size and high pore volume as well as polar pore surface, are anticipated to facilitate $C_2H_2$ adsorption. To examine the effectiveness of the variant electronic state of OMSs on the adsorption performance, we selected $C_2H_2$ as a model gas molecule for evaluation. The $C_2H_2$ adsorption isotherms of both MOFs were measured at 273, 285, and 298 K, respectively (Figures 3B, 3C, S17, S19–S21, and S23–S24). Evidently, LIFM-26(Fe[II]/Fe[III]) showed much higher $C_2H_2$ uptake capacity (181 and 131 $cm^3$ $g^{-1}$ at 273 and 298 K, 1 bar, respectively) than LIFM-27(Fe[III]) (128 and 97 $cm^3$ $g^{-1}$ at 273 and 298 K, 1 bar, respectively), suggesting that Fe[II] center with higher electron density for stronger $\pi$ back donation in LIFM-26(Fe[II]/Fe[III]) can effectively improve its adsorption behavior. Specifically, LIFM-26(Fe[II]/Fe[III]) (17.0 $cm^3$ $g^{-1}$) can take up more than four times of $C_2H_2$ than LIFM-27(Fe[III]) (4.2 $cm^3$ $g^{-1}$) at low pressure (3.4 mbar) (Figure 3D). Moreover, the $C_2H_2$ uptake capacity of LIFM-26(Fe[II]/Fe[III]) is much higher than that of (Fe[II]/Fe[III])$_3$O(TFBDC)$_3$ (Figures 3B and S25), and is also higher than many other known MOFs like Zn-MOF-74 (122 $cm^3$ $g^{-1}$),[31] UTSA-74a (104 $cm^3$ $g^{-1}$),[33] and PCP-33 (122 $cm^3$ $g^{-1}$),[39] but is lower than some MOFs like FJI-H8-R series (174–229 $cm^3$ $g^{-1}$),[17,24] MIL-160 (191 $cm^3$ $g^{-1}$),[40] SIFSIX-Cu-TPA (185 $cm^3$ $g^{-1}$),[41] and FJU-90a (180 $cm^3$ $g^{-1}$) (Table S5).[42] To further confirm the effect of low-valent Fe(II) center, the $C_2H_2$ adsorption of LIFM-27(Fe[III])-EtOH, in which the amount of Fe[II] center is less than the prototypical LIFM-26(Fe[II]/Fe[III]), was measured at 298 K. As expected, the $C_2H_2$ uptake by LIFM-27(Fe[III])-EtOH was lower than LIFM-26(Fe[II]/Fe[III]) but higher than LIFM-27(Fe[III]) (Figures S30–S32). Additionally, the $CO_2$ adsorption isotherms were performed on both Fe-MOFs. LIFM-26(Fe[II]/Fe[III]) can take up 80 $cm^3$ $g^{-1}$ $CO_2$ at 298 K and 1 bar, while the uptake capacity of LIFM-27(Fe[III]) is 51 $cm^3$ $g^{-1}$ under the same condition (Figures 3B, 3C, S18, and S22). These

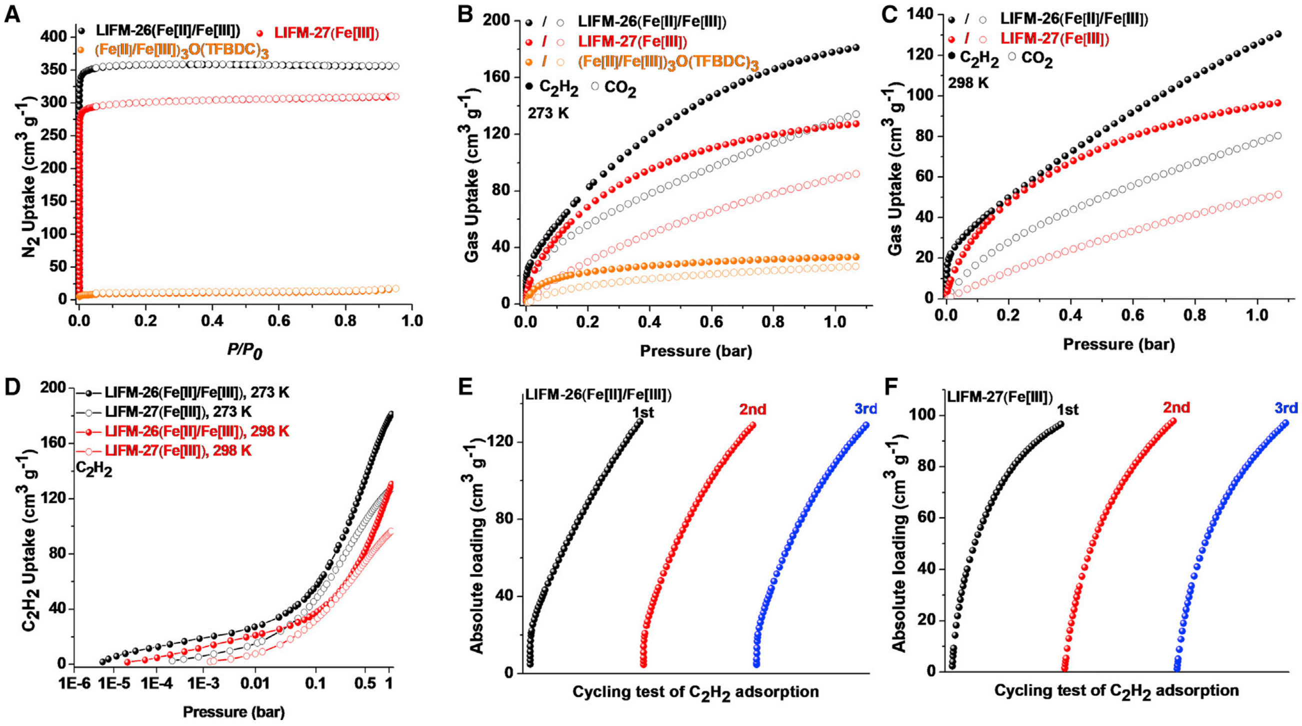

**Figure 3. Gas adsorption properties of the three MOFs**

(A) The $N_2$ adsorption of all the three MOFs at 77 K.

(B and C) The $C_2H_2$ and $CO_2$ adsorption isotherms at (B) 273 and (C) 298 K.

(D) The $C_2H_2$ adsorption isotherms.

(E and F) The repetitive $C_2H_2$ adsorption isotherms of (E) LIFM-26(Fe[II]/Fe[III]) and (F) LIFM-27(Fe[III]).

results indicate that the gas adsorption performance of the two isostructural Fe-MOFs can be finely tuned by regulating the electron state of OMSs. Furthermore, the continuous $C_2H_2$ and $CO_2$ adsorption isotherms on both Fe-MOFs were carefully performed, verifying their excellent reusability (Figures 3E, 3F, and S26–S29).

The isosteric heat ($Q_{st}$) of $C_2H_2$ and $CO_2$ on both MOFs were calculated using the Clausius-Clapeyron equation based on their adsorption isotherms at three different temperatures (Figures S17, S18, S21, S22, and S33–S36). For $C_2H_2$, LIFM-26(Fe[II]/Fe[III]) displays higher isosteric heat (53.8 kJ $mol^{-1}$) than LIFM-27(Fe[III]) (44.6 kJ $mol^{-1}$) at near-zero coverage corresponding to the interactions between gas and Fe center, which further confirms the electronic effect of the open Fe[II] centers (Figures S37 and S38). Afterward, the subsequent gradual decrease in isosteric heat for $C_2H_2$ on both MOFs along with increased $C_2H_2$ loading amount indicate the adsorption saturation of Fe centers. Notably, the moderate $Q_{st}$ value of $C_2H_2$ in LIFM-26(Fe[II]/Fe[III]) is lower than some other reported MOFs with OMSs, such as ATC-Cu (79.1 kJ $mol^{-1}$),[16] Cu@UiO-66$(COOH)_2$ (74.5 kJ $mol^{-1}$),[43] ZJU-74a (65.0 kJ $mol^{-1}$),[44] and NKMOF-1-Ni (60.3 kJ $mol^{-1}$),[45] implying the sufficient adsorption reversibility of the adsorbent owing to the presence of Fe(III) center. For $CO_2$, both MOFs present comparable isosteric heats, giving values of 37.8 (LIFM-26(Fe[II]/Fe[III])) and 35.8 kJ $mol^{-1}$ (LIFM-27(Fe[III])) at near-zero coverage (Figures S37 and S38). The higher $Q_{st}$ value of $C_2H_2$ than $CO_2$ suggests a promising potential of $C_2H_2$ purification from $C_2H_2$/$CO_2$ gas mixture.

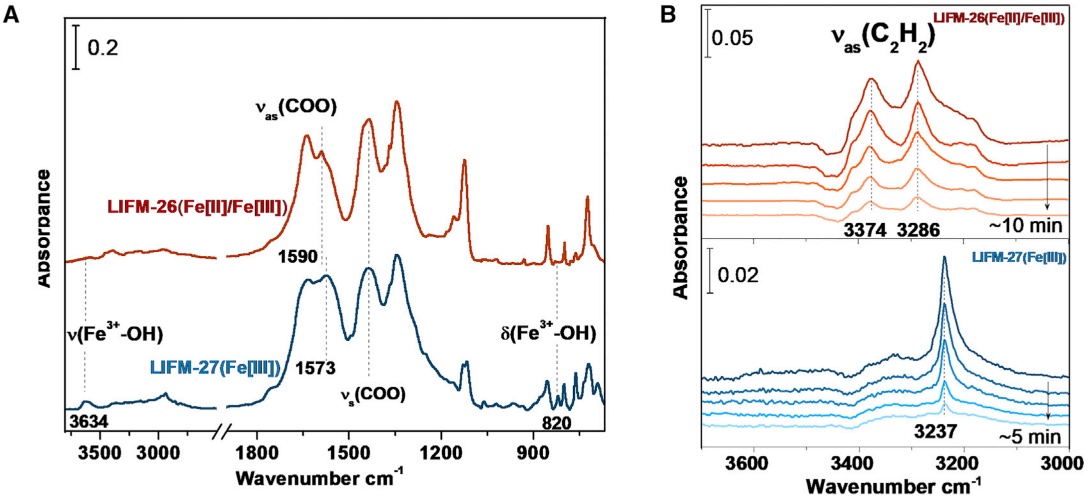

**Figure 4. *In situ* IR spectra of LIFM-26(Fe[II]/Fe[III]) and LIFM-27(Fe[III]) before and after $C_2H_2$ loading**

(A) IR spectra of activated LIFM-26(Fe[II]/Fe[III]) (top) and LIFM-27(Fe[III]) (bottom) samples, referenced to pure KBr pellet in vacuum (<20 mTorr base pressure).

(B) Difference spectra showing the asymmetric stretching band vas of adsorbed $C_2H_2$ in LIFM-26(Fe[II]/Fe[III]) (top) and LIFM-27(Fe[III]) (bottom) samples upon loading at the pressure of ~1 bar (top spectrum in each panel) and subsequent evacuation of gas phase under vacuum for ~10 and ~5 min, respectively. Each is referenced to the spectrum of activated sample.

## Adsorption mechanism

To probe the binding interaction of $C_2H_2$ with the frameworks, *in situ* IR spectroscopy measurements were performed. The samples of LIFM-26(Fe[II]/Fe[III]) and LIFM-27(Fe[III]) were first heated under vacuum to remove trapped solvents and then cooled to room temperature to collect IR spectra of activated samples, as presented in Figure 4A. The spectra of two samples are dominated by the vibrational bands associated with the organic linker (Figure S44), which exhibit general similarities. A noticeable difference is that the LIFM-27(Fe[III]) sample shows extra two bands at ~3,634 and 820 cm$^{-1}$, which are absent in LIFM-26(Fe[II]/Fe[III]). Based on the well-established studies on Fe-based MOFs containing a hydroxyl group,[46,47] these two bands are attributed to the stretching and deformation modes of OH$^-$, which terminates one Fe[III] of the trimeric Fe[III]$_3$O cluster for charge balance. In the neutrally charged (Fe[II]/Fe[III])$_3$O cluster of the LIFM-26(Fe[II]/Fe[III]) sample, no extra OH$^-$ is needed. In addition, careful examination of spectra at 1,600–1,500 cm$^{-1}$ reveals that carboxylate asymmetric stretching band $\nu_{as}$(COO) in LIFM-26(Fe[II]/Fe[III]) occurs at a higher frequency (1,590 cm$^{-1}$) than that in the LIFM-27(Fe[III]) sample, leading to a larger separation $\Delta\nu$ between $\nu_{as}$(COO) and $\nu_s$(COO).[48] This is as expected since the inequivalence of the two C−O bonds connected with Fe[II] and Fe[III], respectively, would further split $\Delta\nu$.[49,50] Gas adsorption measurement was then conducted on these activated samples by loading $C_2H_2$ at ~1 bar for ~10 min to ensure adsorption saturation, which was followed by subsequent desorption via pumping the samples under vacuum. The adsorbed $C_2H_2$ is clearly observed in different IR spectra (Figure 4B), which demonstrate the characteristic stretching band $\nu_{as}$($C_2H_2$) of adsorbed $C_2H_2$ at 3,400–3,200 cm$^{-1}$. A marked difference is noted for both the position and shape of the $\nu_{as}$($C_2H_2$) band between in LIFM-26(Fe[II]/Fe[III]) and LIFM-27(Fe[III]). LIFM-27(Fe[III]) displays only a single band located at 3,237 cm$^{-1}$, which corresponds to $C_2H_2$ adsorbed at the primary exposed Fe[III] sites, as identified by molecular simulations (Figures 5B and S46; vide infra). In comparison, LIFM-26(Fe[II]/Fe[III]) shows two distinct bands appearing at higher frequencies of 3,374 and 3,286 cm$^{-1}$, pointing to two types of $C_2H_2$

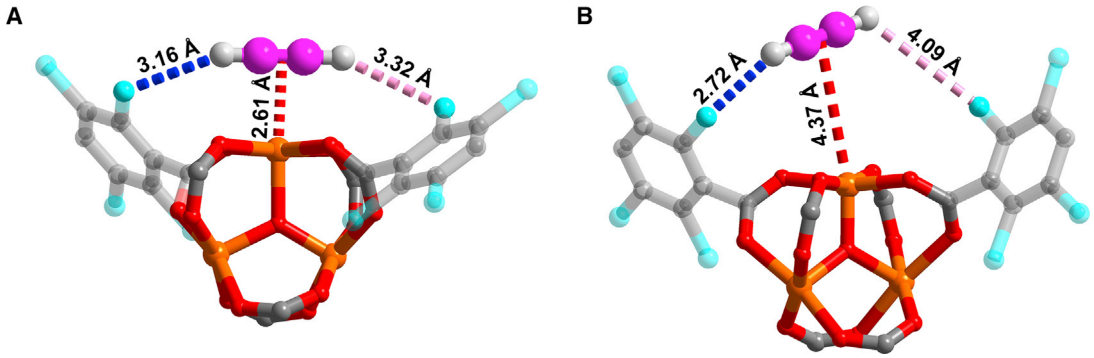

**Figure 5. Preferential binding sites**

(A and B) The preferential $C_2H_2$ binding sites in (A) LIFM-26(Fe[II]/Fe[III]) and (B) LIFM-27(Fe[III]).

adsorbed on Fe[II] and Fe[III] sites, respectively. It is noteworthy that the 3,374 $cm^{-1}$ band undergoes an upward shift (blue shift) with respect to the value of the gas phase $C_2H_2$ (3,287 $cm^{-1}$).[51] Such a shift to the higher wavenumber strongly suggests that π back donation occurs between Fe[II] cations and $C_2H_2$ in LIFM-26(Fe[II]/Fe[III]),[52] which weakens the C–C bond but stiffens the C–H bond,[53] thus resulting in a raise of C–H stretching frequency. The broadening and asymmetric line shape of the $v_{as}(C_2H_2)$ bands in LIFM-26(Fe[II]/Fe[III]) indicate vibrational dynamic coupling between adsorbed $C_2H_2$ molecules, which could account for the occurrence of the Fe[III]-bound $C_2H_2$ band at a higher frequency of 3,286 $cm^{-1}$ in LIFM-26(Fe[II]/Fe[III]) compared with that in LIFM-27(Fe[III]) (3,237 $cm^{-1}$).[54]

To get further insight into the adsorption mechanism with regard to the mixed-valent Fe[II]/Fe[III] centers, we implemented molecular simulations. For LIFM-26(Fe[II]/Fe[III]), $C_2H_2$ is mainly located in the channel surrounded by one open Fe[II] center and two chlorine atoms, in which the strong Fe···C≡C (2.61 Å) and weak C-Cl···H interactions (3.16 and 3.22 Å) occur between $C_2H_2$ and the framework, suggesting strong $C_2H_2$ binding affinity (Figures 5A and S45), whereas the $C_2H_2$ binding site in LIFM-27(Fe[III]) is located in the elliptic channel surrounded by one open Fe[III] center and two chlorine atoms with weak Fe··· C≡C (4.37 Å) and C-Cl···H interactions (2.72 and 4.09 Å), indicating weaker $C_2H_2$ binding affinity compared with LIFM-26(Fe[II]/Fe[III]) (Figures 5B and S46). The calculated $C_2H_2$ binding energy for LIFM-26(Fe[II]/Fe[III]) is 49.7 kJ $mol^{-1}$, which is higher than LIFM-27(Fe[III]) (45.6 kJ $mol^{-1}$) (Table S6), manifesting the stronger interaction between $C_2H_2$ and LIFM-26(Fe[II]/Fe[III]). In comparison, both LIFM-26(Fe[II]/Fe[III]) and LIFM-27(Fe[III]) present weaker interactions toward $CO_2$. The observed $CO_2$ binding site in LIFM-26(Fe[II]/Fe[III]) is mainly the Fe···O-C interaction with a distance of 2.13 Å, which is similar to that of LIFM-27(Fe[III]) (Fe···O-C distance is 2.17 Å) (Figures S47–S49). The $CO_2$ binding energy for LIFM-26(Fe[II]/Fe[III]) and LIFM-27(Fe[III]) are calculated to be 38.5 and 37.6 kJ $mol^{-1}$, respectively (Table S6), which are weaker than those of $C_2H_2$, confirming the feasible $C_2H_2/CO_2$-separation performance.

## IAST adsorption selectivity and dynamic breakthrough

To evaluate the $C_2H_2/CO_2$-separation ability, the IAST[55] calculation was conducted on the basis of the composition of a 50:50 $C_2H_2/CO_2$ mixture (Figures S39–S42). As shown in Figures 6A and S43, LIFM-26(Fe[II]/Fe[III]) gives much higher $C_2H_2/CO_2$ selectivity (56.1 at 0.01 bar) than LIFM-27(Fe[III]) (14.3 at 0.01 bar) under low pressure, which can be attributed to the stronger Fe[II]–$C_2H_2$ binding affinity as a result

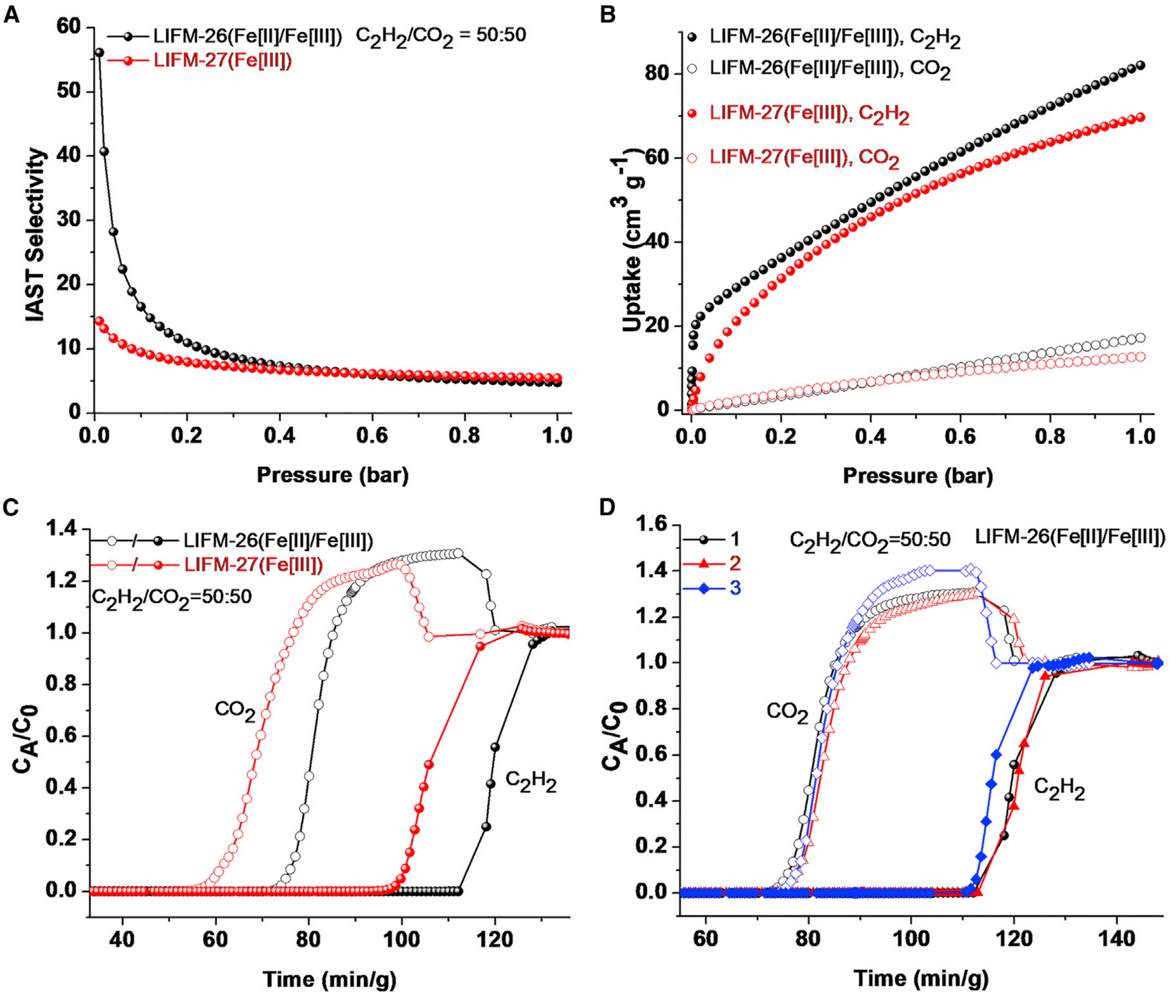

**Figure 6. IAST calculated selectivity and dynamic breakthrough**

(A) IAST adsorption selectivity of $C_2H_2/CO_2$ (v/v, 50:50) at 298 K.

(B) IAST calculated $C_2H_2$ and $CO_2$ uptake capacity for equimolar $C_2H_2/CO_2$ mixtures.

(C) The experimental dynamic breakthrough measurements of LIFM-26(Fe[II]/Fe[III]) and LIFM-27(Fe[III]) for $C_2H_2/CO_2$ mixture at 298 K and 1 bar.

(D) The cycling dynamic breakthrough measurements of LIFM-26(Fe[II]/Fe[III]) for $C_2H_2/CO_2$ mixture at 298 K and 1 bar.

of the increased electron density at the Fe[II] center. Subsequently, the $C_2H_2/CO_2$ selectivity for both MOFs gradually decreases as a function of the increased pressure due to the adsorption saturation of the Fe centers. The final $C_2H_2/CO_2$ selectivities for LIFM-26(Fe[II]/Fe[III]) and LIFM-27(Fe[III]) are 4.8 and 5.5 at 298 K and 1 bar, respectively, which are comparable with many reported MOFs, such as SIFSIX-Cu-TPA (5.3),[41] SNNU-45 (4.5),[56] TIFSIX-2-Cu-i (6.5),[28] FJU-90 (4.3),[42] UTSA-222 (4.0),[57] JNU-1 (3.6),[18] and Zn-MOF-74 (2.8).[31] Additionally, the $C_2H_2$ uptake capacity was calculated based on the IAST method. Compared with LIFM-27(Fe[III]) (4.7 $cm^3$ $g^{-1}$ at 0.01 bar), LIFM-26(Fe[II]/Fe[III]) exhibits enhanced $C_2H_2$-capture performance, especially at low pressure (20.4 $cm^3$ $g^{-1}$ at 0.01 bar) (Figure 6B). More importantly, the $C_2H_2$ uptake capacity for both MOFs is remarkably higher than their $CO_2$ adsorption, implying potential $C_2H_2$-separation ability from $C_2H_2/CO_2$ mixture (Figure 6B).

Prompted by the outstanding $C_2H_2$ uptake capacity and $C_2H_2/CO_2$ adsorption selectivity, the simulated transient breakthrough experiments were carried out according to the documented methodology.[58] For both LIFM-26(Fe[II]/Fe[III]) and LIFM-27(Fe[III]), $CO_2$ elutes first, and then $C_2H_2$ breaks through after some time, demonstrating the adequate capacity for the demanding $C_2H_2/CO_2$ separation (Figures S52 and S53). The $C_2H_2$ capture productivity calculated on the basis of the simulated breakthrough curves gives rise to the values of 88.9 (LIFM-26(Fe[II]/Fe[III])) and 76.6 (LIFM-27(Fe[III])) $cm^3\ g^{-1}$, unveiling the better $C_2H_2/CO_2$-separation performance of LIFM-26(Fe[II]/Fe[III]). It is noticeable that the $C_2H_2$ productivity for LIFM-26(Fe[II]/Fe[III]) is slightly lower than FJU-90 (114.2 $cm^3\ g^{-1}$)[42] yet higher than other reported MOFs including FJU-22a (83.1 $cm^3\ g^{-1}$),[59] ZUL-60a (80.6 $cm^3\ g^{-1}$),[60] UTSA-74a (79.7 $cm^3\ g^{-1}$),[33] Zn-MOF-74 (76.6 $cm^3\ g^{-1}$),[31] and PCP-33 (75.7 $cm^3\ g^{-1}$).[39]

To further assess the practical $C_2H_2/CO_2$-separation performance by both LIFM-26(Fe[II]/Fe[III]) and LIFM-27(Fe[III]), dynamic fixed-bed breakthrough experiments were conducted through a stainless-steel column under ambient condition, in which the equimolar $C_2H_2/CO_2$ mixture flowed over the packed column with a flow rate of 1.0 mL $min^{-1}$. As depicted in Figure 6C, both Fe-MOFs present excellent $C_2H_2$-separation performance from $C_2H_2/CO_2$ mixture. For LIFM-26(Fe[II]/Fe[III]), $CO_2$ undoubtedly elutes first and then quickly reaches a pure grade without detectable $C_2H_2$, while $C_2H_2$ remains in the packed column for a remarkable time until it is saturated in LIFM-26(Fe[II]/Fe[III]). As expected, LIFM-27(Fe[III]) exhibits similar $C_2H_2/CO_2$ dynamic breakthrough behavior but with a shorter $C_2H_2$ breakthrough time. Based on the experimental breakthrough curves, LIFM-26(Fe[II]/Fe[III]) and LIFM-27(Fe[III]) present comparable $C_2H_2/CO_2$ selectivity with values of 1.6 and 1.7, respectively. The calculated $C_2H_2$-capture productivity for LIFM-26(Fe[II]/Fe[III]) based on the experimental breakthrough curve is estimated to be 60.0 $cm^3\ g^{-1}$, whereas the value for LIFM-27(Fe[III]) is 53.7 $cm^3\ g^{-1}$. In principle, ideal adsorbents should present good recyclability in practical industrial applications. Therefore, the continuous dynamic breakthrough experiments were performed under the above conditions. The results indicate that both Fe-MOFs maintain almost the same retaining time and capture productivity in three continuous $C_2H_2/CO_2$ dynamic breakthrough experiments (Figures 6D, S50, and S51), demonstrating their good reusability. The PXRD patterns after the repetitive experiments also confirm the crystallinity is retained well (Figures S54 and S55). Taken together, these results clearly demonstrate that the Fe-MOFs have successfully achieved a combination of high $C_2H_2$ uptake capacity, moderate-high $C_2H_2/CO_2$ selectivity, and sufficient reversibility by rationally regulating the electronic state of the open-metal centers.

In summary, a metal electronic-state manipulation strategy has been successfully applied to constructing a pair of microporous isostructural Fe-MOFs featuring open Fe centers with different electron densities for efficient $C_2H_2/CO_2$ separation. Notably, the isostructural LIFM-26(Fe[II]/Fe[III]) and LIFM-27(Fe[III]) can be interconverted, and the electronic state of Fe centers can be finely tuned by simply changing the oxidation conditions depending on the solvents and reaction time, thus facilitating understanding of the inherent relationship between the metal electronic state and $C_2H_2$ selective adsorption. Compared with LIFM-27(Fe[III]), LIFM-26(Fe[II]/Fe[III]) presents remarkably higher $C_2H_2$ uptake capacity while retaining moderate-high $C_2H_2/CO_2$ selectivity, which is well supported by the simulated and experimental dynamic breakthrough experiments. *In situ* IR and molecular calculations manifest that LIFM-26(Fe[II]/Fe[III]) exhibits enhanced binding affinity toward $C_2H_2$ than LIFM-27(Fe[III]) due to the increased electron density at the metal site, resulting in a stronger $\pi$ back donation. Significantly, this work provides an effective guideline to realize the challenging $C_2H_2/CO_2$ separation by rationally manipulating the electronic state of OMSs in MOF pore spaces.

## MATERIALS AND METHODS

See the supplemental experimental procedures for full details of synthesis, characterization, modeling and analysis, and adsorption and breakthrough measurements.

## EXPERIMENTAL PROCEDURES

### Resource availability

*Lead contact*

Further information and requests for resources should be directed to and will be fulfilled by the lead contact, Cheng-Yong Su (cesscy@mail.sysu.edu.cn), and Shengqian Ma (shengqian.ma@unt.edu).

*Materials availability*

All materials generated in this study are available from the lead contact without restriction.

*Data and code availability*

The X-ray crystallographic coordinates for LIFM-27(Fe[III]) have been deposited at the Cambridge Crystallographic Data Centre (CCDC) under CCDC: 2114493. These data can be obtained free of charge from the CCDC via http://www.ccdc.cam.ac.uk/data_request/cif. All other data are available from the lead contact upon request.

## SUPPLEMENTAL INFORMATION

Supplemental information can be found online at https://doi.org/10.1016/j.xcrp.2022.100977.

## ACKNOWLEDGMENTS

This work was supported by NSFC (21821003, 21890380, and 22001271), the Chinese Postdoctoral Science Foundation (2017M622866), the International Postdoctoral Exchange Fellowship Program (20180055), and FRF for the Central Universities (20lgpy79). The authors also extend their appreciation to the Robert A. Welch Foundation (B-0027) and Researchers Supporting Program (RSP-2022/55) at King Saud University, Riyadh, Saudi Arabia, for partial support of this work. T.P. and K.A.F. acknowledge the use of services provided by Research Computing at the University of South Florida. The IR spectroscopic work was supported by the US Department of Energy, Office of Science, Basic Energy Sciences, under award no. DE-SC0019902.

## AUTHOR CONTRIBUTIONS

Conceptualization, C.-X.C., C.-Y.S., and S.M.; methodology, C.-X.C.; investigation, C.-X.C.; theoretical calculation, T.P. and K.A.F.; *in situ* IR measurements, K.T.; simulated transient breakthrough, R.K.; Mössbauer spectra, S.C. and L.W.; writing – original draft, C.-X.C.; writing – review & editing, C.-X.C., H.W., S.M., and C.-Y.S.; funding acquisition, C.-X.C., C.-Y.S., and S.M.; all authors analyzed and discussed the data and contributed to writing the paper.

## DECLARATION OF INTERESTS

The authors declare no competing interests.

Received: April 14, 2022
Revised: June 3, 2022
Accepted: June 17, 2022
Published: July 20, 2022

## REFERENCES

1. Sholl, D.S., and Lively, R.P. (2016). Seven chemical separations to change the world. Nature *532*, 435–437. https://doi.org/10.1038/532435a.

2. Guo, C.J., Shen, D., and Bülow, M. (2001). 18-O-03-Kinetic separation of binary mixtures of carbon dioxide and $C_2$ hydrocarbons on modified LTA-type zeolites. In Studies in Surface Science and Catalysis, A. Galarneau, F. Fajula, F. Di Renzo, and J. Vedrine, eds. (Elsevier), p. 144.

3. Pässler, P., Hefner, W., Buckl, K., Meinass, H., Meiswinkel, A., Wernicke, H.-J., Ebersberg, G., Müller, R., Bässler, J., Behringer, H., and Mayer, D. (2011). In Ullmann's Encyclopedia of Industrial Chemistry, B. Elvers, ed. (Wiley-VCH).

4. Duan, X., Cai, J., Yu, J., Wu, C., Cui, Y., Yang, Y., and Qian, G. (2013). Three-dimensional copper (II) metal–organic framework with open metal sites and anthracene nucleus for highly selective $C_2H_2/CH_4$ and $C_2H_2/CO_2$ gas separation at room temperature. Microporous Mesoporous Mater. *181*, 99–104. https://doi.org/10.1016/j.micromeso.2013.07.019.

5. Reid, C.R., and Thomas, K.M. (2001). Adsorption kinetics and size exclusion properties of probe molecules for the selective porosity in a carbon molecular sieve used for air separation. J. Phys. Chem. B *105*, 10619–10629. https://doi.org/10.1021/jp0108263.

6. Adil, K., Belmabkhout, Y., Pillai, R.S., Cadiau, A., Bhatt, P.M., Assen, A.H., Maurin, G., and Eddaoudi, M. (2017). Gas/vapour separation using ultra-microporous metal-organic frameworks: insights into the structure/separation relationship. Chem. Soc. Rev. *46*, 3402–3430. https://doi.org/10.1039/c7cs00153c.

7. Shekhah, O., Chernikova, V., Belmabkhout, Y., and Eddaoudi, M. (2018). Metal–organic framework membranes: from fabrication to gas separation. Crystals *8*, 412. https://doi.org/10.3390/cryst8110412.

8. Yang, L., Qian, S., Wang, X., Cui, X., Chen, B., and Xing, H. (2020). Energy-efficient separation alternatives: metal-organic frameworks and membranes for hydrocarbon separation. Chem. Soc. Rev. *49*, 5359–5406. https://doi.org/10.1039/c9cs00756c.

9. Li, J., Bhatt, P.M., Li, J., Eddaoudi, M., and Liu, Y. (2020). Recent progress on microfine design of metal-organic frameworks: structure regulation and gas sorption and separation. Adv. Mater. *32*, 2002563. https://doi.org/10.1002/adma.202002563.

10. Wang, H., Liu, Y., and Li, J. (2020). Designer metal-organic frameworks for size-exclusion-based hydrocarbon separations: progress and challenges. Adv. Mater. *32*, 2002603. https://doi.org/10.1002/adma.202002603.

11. Lin, R.-B., Xiang, S., Zhou, W., and Chen, B. (2020). Microporous metal-organic framework materials for gas separation. Chem *6*, 337–363. https://doi.org/10.1016/j.chempr.2019.10.012.

12. Hua, G.F., Xie, X.J., Lu, W., and Li, D. (2020). Optimizing supramolecular interactions in metal-organic frameworks for $C_2$ separation. Dalton Trans. *49*, 15548–15559. https://doi.org/10.1039/d0dt03013a.

13. Cui, W.G., Hu, T.L., and Bu, X.H. (2020). Metal-organic framework materials for the separation and purification of light hydrocarbons. Adv. Mater. *32*, 1806445. https://doi.org/10.1002/adma.201806445.

14. Oktawiec, J., Jiang, H.Z.H., Vitillo, J.G., Reed, D.A., Darago, L.E., Trump, B.A., Bernales, V., Li, H., Colwell, K.A., Furukawa, H., et al. (2020). Negative cooperativity upon hydrogen bond-stabilized O2 adsorption in a redox-active metal-organic framework. Nat. Commun. *11*, 3087. https://doi.org/10.1038/s41467-020-16897-z.

15. Reed, D.A., Xiao, D.J., Gonzalez, M.I., Darago, L.E., Herm, Z.R., Grandjean, F., and Long, J.R. (2016). Reversible CO scavenging via adsorbate-dependent spin state transitions in an iron(II)-Triazolate metal-organic framework. J. Am. Chem. Soc. *138*, 5594–5602. https://doi.org/10.1021/jacs.6b00248.

16. Niu, Z., Cui, X., Pham, T., Verma, G., Lan, P.C., Shan, C., Xing, H., Forrest, K.A., Suepaul, S., Space, B., et al. (2021). A MOF-based ultra-strong acetylene nano-trap for highly efficient $C_2H_2/CO_2$ separation. Angew. Chem. Int. Ed. *60*, 5283–5288. https://doi.org/10.1002/anie.202016225.

17. Di, Z., Liu, C., Pang, J., Chen, C., Hu, F., Yuan, D., Wu, M., and Hong, M. (2021). Cage-like porous materials with simultaneous high $C_2H_2$ storage and excellent $C_2H_2/CO_2$ separation performance. Angew. Chem. Int. Ed. *60*, 10828–10832. https://doi.org/10.1002/anie.202101907.

18. Zeng, H., Xie, M., Huang, Y.L., Zhao, Y., Xie, X.J., Bai, J.P., Wan, M.Y., Krishna, R., Lu, W., and Li, D. (2019). Induced fit of $C_2H_2$ in a flexible MOF through cooperative action of open metal sites. Angew. Chem. Int. Ed. *58*, 8515–8519. https://doi.org/10.1002/anie.201904160.

19. Fischer, M., Hoffmann, F., and Fröba, M. (2010). New microporous materials for acetylene storage and $C_2H_2/CO_2$ separation: insights from molecular simulations. ChemPhysChem *11*, 2220–2229. https://doi.org/10.1002/cphc.201000126.

20. Xu, H., He, Y., Zhang, Z., Xiang, S., Cai, J., Cui, Y., Yang, Y., Qian, G., and Chen, B. (2013). A microporous metal–organic framework with both open metal and Lewis basic pyridyl sites for highly selective C2H2/CH4and $C_2H_2/CO_2$ gas separation at room temperature. J. Mater. Chem. *1*, 77–81. https://doi.org/10.1039/c2ta00155a.

21. Ji, Y., Ding, L., Cheng, Y., Zhou, H., Yang, S., Li, F., and Li, Y. (2017). Understanding the effect of ligands on C2H2 storage and $C_2H_2/CH_4$, $C_2H_2/CO_2$ separation in metal–organic frameworks with open Cu(II) sites. J. Phys. Chem. C *121*, 24104–24113.

22. Moreau, F., da Silva, I., Al Smail, N.H., Easun, T.L., Savage, M., Godfrey, H.G.W., Parker, S.F., Manuel, P., Yang, S., and Schröder, M. (2017). Unravelling exceptional acetylene and carbon dioxide adsorption within a tetra-amide functionalized metal-organic framework. Nat. Commun. *8*, 14085. https://doi.org/10.1038/ncomms14085.

23. Chen, S., Behera, N., Yang, C., Dong, Q., Zheng, B., Li, Y., Tang, Q., Wang, Z., Wang, Y., and Duan, J. (2020). A chemically stable nanoporous coordination polymer with fixed and free $Cu^{2+}$ ions for boosted $C_2H_2/CO_2$ separation. Nano Res. *14*, 546–553. https://doi.org/10.1007/s12274-020-2935-1.

24. Pang, J., Jiang, F., Wu, M., Liu, C., Su, K., Lu, W., Yuan, D., and Hong, M. (2015). A porous metal-organic framework with ultrahigh acetylene uptake capacity under ambient conditions. Nat. Commun. *6*, 7575. https://doi.org/10.1038/ncomms8575.

25. Lin, R.-B., Li, L., Wu, H., Arman, H., Li, B., Lin, R.-G., Zhou, W., and Chen, B. (2017). Optimized separation of acetylene from carbon dioxide and ethylene in a microporous material. Material. J. Am. Chem. Soc. *139*, 8022–8028. https://doi.org/10.1021/jacs.7b03850.

26. Bloch, E.D., Queen, W.L., Krishna, R., Zadrozny, J.M., Brown, C.M., and Long, J.R. (2012). Hydrocarbon separations in a metal-organic framework with open iron(II) coordination sites. Science *335*, 1606–1610. https://doi.org/10.1126/science.1217544.

27. Zhang, J.-P., and Chen, X.-M. (2009). Optimized acetylene/carbon dioxide sorption in a dynamic porous crystal. J. Am. Chem. Soc. *131*, 5516–5521. https://doi.org/10.1021/ja8089872.

28. Chen, K.-J., Scott, H.S., Madden, D.G., Pham, T., Kumar, A., Bajpai, A., Lusi, M., Forrest, K.A., Space, B., Perry, J.J., and Zaworotko, M.J. (2016). Benchmark $C_2H_2/CO_2$ and $CO_2/C_2H_2$ separation by two closely related hybrid ultra-microporous materials. Chem *1*, 753–765. https://doi.org/10.1016/j.chempr.2016.10.009.

29. Cui, X., Chen, K., Xing, H., Yang, Q., Krishna, R., Bao, Z., Wu, H., Zhou, W., Dong, X., Han, Y., et al. (2016). Pore chemistry and size control in hybrid porous materials for acetylene capture from ethylene. Science *353*, 141–144. https://doi.org/10.1126/science.aaf2458.

30. Fan, W., Yuan, S., Wang, W., Feng, L., Liu, X., Zhang, X., Wang, X., Kang, Z., Dai, F., Yuan, D., et al. (2020). Optimizing multivariate metal-organic frameworks for efficient $C_2H_2/CO_2$ separation. J. Am. Chem. Soc. *142*, 8728–8737. https://doi.org/10.1021/jacs.0c00805.

31. Xiang, S., Zhou, W., Zhang, Z., Green, M.A., Liu, Y., and Chen, B. (2010). Open metal sites within isostructural metal-organic frameworks for differential recognition of acetylene and extraordinarily high acetylene storage capacity at room temperature. Angew. Chem. Int. Ed. *49*, 4615–4618. https://doi.org/10.1002/anie.201000094.

32. Yoon, J.W., Lee, J.S., Lee, S., Cho, K.H., Hwang, Y.K., Daturi, M., Jun, C.H., Krishna, R., and Chang, J.S. (2015). Adsorptive separation of acetylene from light hydrocarbons by mesoporous iron trimesate MIL-100(Fe). Chem. Eur J. *21*, 18431–18438. https://doi.org/10.1002/chem.201502893.

33. Luo, F., Yan, C., Dang, L., Krishna, R., Zhou, W., Wu, H., Dong, X., Han, Y., Hu, T.L., O'Keeffe,

M., et al. (2016). UTSA-74: a MOF-74 isomer with two accessible binding sites per metal center for highly selective gas separation. J. Am. Chem. Soc. *138*, 5678–5684. https://doi.org/10.1021/jacs.6b02030.

34. Yoon, J.W., Seo, Y.K., Hwang, Y.K., Chang, J.S., Leclerc, H., Wuttke, S., Bazin, P., Vimont, A., Daturi, M., Bloch, E., et al. (2010). Controlled reducibility of a metal-organic framework with coordinatively unsaturated sites for preferential gas sorption. Angew. Chem. Int. Ed. *49*, 5949–5952. https://doi.org/10.1002/anie.201001230.

35. Bachman, J.E., Kapelewski, M.T., Reed, D.A., Gonzalez, M.I., and Long, J.R. (2017). $M_2$(m-dobdc) (M = Mn, Fe, Co, Ni) metal-organic frameworks as highly selective, high-capacity adsorbents for olefin/paraffin separations. J. Am. Chem. Soc. *139*, 15363–15370. https://doi.org/10.1021/jacs.7b06397.

36. Luna-Triguero, A., Vicent-Luna, J.M., Madero-Castro, R.M., Gómez-Álvarez, P., and Calero, S. (2019). Acetylene storage and separation using metal-organic frameworks with open metal sites. ACS Appl. Mater. Interfaces *11*, 31499–31507. https://doi.org/10.1021/acsami.9b09010.

37. Chen, C.X., Zheng, S.P., Wei, Z.W., Cao, C.C., Wang, H.P., Wang, D.W., Jiang, J.J., Fenske, D.T., and Su, C.Y. (2017). A robust metal-organic framework combining open metal sites and polar groups for methane purification and $CO_2$/fluorocarbon capture. Chem. Eur J. *23*, 4060–4064. https://doi.org/10.1002/chem.201606038.

38. Yoon, J.H., Choi, S.B., Oh, Y.J., Seo, M.J., Jhon, Y.H., Lee, T.-B., Kim, D., Choi, S.H., and Kim, J. (2007). A porous mixed-valent iron MOF exhibiting the acs net: synthesis, characterization and sorption behavior of $Fe_3O(F_4BDC)_3(H_2O)_3\cdot(DMF)_{3.5}$. Catal. Today *120*, 324–329. https://doi.org/10.1016/j.cattod.2006.09.003.

39. Duan, J., Jin, W., and Krishna, R. (2015). Natural gas purification using a porous coordination polymer with water and chemical stability. Inorg. Chem. *54*, 4279–4284. https://doi.org/10.1021/ic5030058.

40. Ye, Y., Xian, S., Cui, H., Tan, K., Gong, L., Liang, B., Pham, T., Pandey, H., Krishna, R., Lan, P.C., et al. (2022). Metal–organic framework based hydrogen-bonding nanotrap for efficient acetylene storage and separation. J. Am. Chem. Soc. *144*, 1681–1689. https://doi.org/10.1021/jacs.1c10620.

41. Li, H., Liu, C., Chen, C., Di, Z., Yuan, D., Pang, J., Wei, W., Wu, M., and Hong, M. (2021). An unprecedented pillar-cage fluorinated hybrid porous framework with highly efficient acetylene storage and separation. Angew. Chem. Int. Ed. *60*, 7547–7552. https://doi.org/10.1002/anie.202013988.

42. Ye, Y., Ma, Z., Lin, R.B., Krishna, R., Zhou, W., Lin, Q., Zhang, Z., Xiang, S., and Chen, B. (2019). Pore space partition within a metal-organic framework for highly efficient $C_2H_2$/$CO_2$ separation. J. Am. Chem. Soc. *141*, 4130–4136. https://doi.org/10.1021/jacs.9b00232.

43. Zhang, L., Jiang, K., Yang, L., Li, L., Hu, E., Yang, L., Shao, K., Xing, H., Yang, Y., Cui, Y., et al. (2021). Benchmark $C_2H_2$/$CO_2$ separation in an ultramicroporous metal–organic framework via copper(I)-Alkynyl chemistry. Angew. Chem. Int. Ed. *60*, 15995–16002. https://doi.org/10.1002/anie.202102810.

44. Pei, J., Shao, K., Wang, J.X., Wen, H.M., Yang, Y., Cui, Y., Krishna, R., Li, B., and Qian, G. (2020). A chemically stable hofmann-type metal-organic framework with sandwich-like binding sites for benchmark acetylene capture. Adv. Mater. *32*, 1908275. https://doi.org/10.1002/adma.201908275.

45. Peng, Y.-L., Pham, T., Li, P., Wang, T., Chen, Y., Chen, K.-J., Forrest, K.A., Space, B., Cheng, P., Zaworotko, M.J., and Zhang, Z. (2018). Robust ultramicroporous metal–organic frameworks with BenchmarkAffinity forAcetylene. Angew. Chem. Int. Ed. *57*, 10971–10975. https://doi.org/10.1002/anie.201806732.

46. Xiao, D.J., Bloch, E.D., Mason, J.A., Queen, W.L., Hudson, M.R., Planas, N., Borycz, J., Dzubak, A.L., Verma, P., Lee, K., et al. (2014). Oxidation of ethane to ethanol by N2O in a metal–organic framework with coordinatively unsaturated iron(II) sites. Nat. Chem. *6*, 590–595. https://doi.org/10.1038/nchem.1956.

47. Devic, T., Horcajada, P., Serre, C., Salles, F., Maurin, G., Moulin, B., Heurtaux, D., Clet, G., Vimont, A., Grenèche, J.M., et al. (2010). Functionalization in flexible porous solids: effects on the pore opening and the Host−Guest interactions. J. Am. Chem. Soc. *132*, 1127–1136. https://doi.org/10.1021/ja9092715.

48. Deacon, G.B., and Phillips, R.J. (1980). Relationships between the carbon-oxygen stretching frequencies of carboxylato complexes and the type of carboxylate coordination. Coord. Chem. Rev. *33*, 227–250. https://doi.org/10.1016/s0010-8545(00)80455-5.

49. Nakamoto, K. (2009). Infrared and Raman Spectra of Inorganic and Coordination Compounds, Sixth edition (Wiley & Sons, Inc.).

50. Colthup, N.B., Daly, L.H., and Wiberley, S.E. (1990). Introduction to Infrared and Raman Spectroscopy, Third edition (Academic Press).

51. Kumar, N., Mukherjee, S., Harvey-Reid, N.C., Bezrukov, A.A., Tan, K., Martins, V., Vandichel, M., Pham, T., van Wyk, L.M., Oyekan, K., et al. (2021). Breaking the trade-off between selectivity and adsorption capacity for gas separation. Chem *7*, 3085–3098. https://doi.org/10.1016/j.chempr.2021.07.007.

52. Citek, C., Oyala, P.H., and Peters, J.C. (2019). Mononuclear Fe(I) and Fe(II) acetylene adducts and their reductive protonation to terminal Fe(IV) and Fe(V) carbynes. J. Am. Chem. Soc. *141*, 15211–15221. https://doi.org/10.1021/jacs.9b06987.

53. Lamberti, C., Zecchina, A., Groppo, E., and Bordiga, S. (2010). Probing the surfaces of heterogeneous catalysts by in situ IR spectroscopy. Chem. Soc. Rev. *39*, 4951. https://doi.org/10.1039/c0cs00117a.

54. Tobin, R.G. (1987). Vibrational linewidths of adsorbed molecules: experimental considerations and results. Surf. Sci. *183*, 226–250. https://doi.org/10.1016/s0039-6028(87)80347-3.

55. Myers, A.L., and Prausnitz, J.M. (1965). Thermodynamics of mixed-gas adsorption. AIChE J. *11*, 121–127. https://doi.org/10.1002/aic.690110125.

56. Li, Y.P., Wang, Y., Xue, Y.Y., Li, H.P., Zhai, Q.G., Li, S.N., Jiang, Y.C., Hu, M.C., and Bu, X. (2019). Ultramicroporous building units as a path to Bi-microporous metal-organic frameworks with high acetylene storage and separation performance. Angew. Chem. Int. Ed. *58*, 13590–13595. https://doi.org/10.1002/anie.201908378.

57. Ma, J.X., Guo, J., Wang, H., Li, B., Yang, T., and Chen, B. (2017). Microporous lanthanide metal-organic framework constructed from lanthanide metalloligand for selective separation of C2H2/CO2 and C2H2/CH4 at room temperature. Inorg. Chem. *56*, 7145–7150. https://doi.org/10.1021/acs.inorgchem.7b00762.

58. Krishna, R. (2017). Screening metal–organic frameworks for mixture separations in fixed-bed adsorbers using a combined selectivity/capacity metric. RSC Adv. *7*, 35724–35737. https://doi.org/10.1039/c7ra07363a.

59. Yao, Z., Zhang, Z., Liu, L., Li, Z., Zhou, W., Zhao, Y., Han, Y., Chen, B., Krishna, R., and Xiang, S. (2016). Extraordinary separation of acetylene-containing mixtures with microporous metal–organic frameworks with open O donor sites and tunable robustness through control of the helical chain secondary building units. Chem. Eur J. *22*, 5676–5683. https://doi.org/10.1002/chem.201505107.

60. Duan, X., Zhang, Q., Cai, J., Yang, Y., Cui, Y., He, Y., Wu, C., Krishna, R., Chen, B., and Qian, G. (2014). A new metal–organic framework with potential for adsorptive separation of methane from carbon dioxide, acetylene, ethylene, and ethane established by simulated breakthrough experiments. J. Mater. Chem. *2*, 2628. https://doi.org/10.1039/c3ta14454b.